Interference effects in the photoelectron spectrum of the NeKr dimer and vibrationally selected interatomic Coulombic decay

Jacqueline Fedyk,[1,*] Kirill Gokhberg,[1] Tsveta Miteva,[2] Lorenz S. Cederbaum,[1] and Alexander I. Kuleff[1]

[1]*Theoretische Chemie, Physikalisch-Chemisches Institut, Universität Heidelberg, Im Neuenheimer Feld 229, D-69120 Heidelberg, Germany*

[2]*Laboratoire de Chimie Physique-Matière et Rayonnement, UMR 7614, Sorbonne Université, CNRS, 75005 Paris, France*

(Received 21 November 2022; accepted 30 January 2023; published 16 February 2023)

In our work we study the interatomic Coulombic decay (ICD) in the NeKr dimer, where after 2*s* ionization of the Ne, the system relaxes and the excess energy is utilized to ionize the Kr. The temporal evolution of the ICD process in NeKr has been recently measured and theoretically explained by Trinter *et al.* [Chem. Sci. **13**, 1789 (2022)]. Here we focus on two other main goals. The first goal regards the found interference effects in the photoemission (PE) spectrum, which are unusual phenomena in noble gas dimers. They result from the coherently excited vibrational energy levels and substantial dependence of the large ICD decay width on the internuclear distance. The PE spectrum reacts sensitively to changes in the potential energy curve (PEC) of the 2*s* ionized state, and we modified the available *ab initio* PEC in such a way that satisfactory agreement between theoretical and experimental data is achieved. The impact of isotope masses on the PE spectrum is briefly discussed and used in the determination of the PEC. Our second main goal concerns the nuclear motion during the ICD process. Here we investigate the impact of different vibrationally excited states of the electronic ground state on the ICD-electron and kinetic energy release (KER) spectra. To transfer our vibrationally selected ICD model to a realizable experiment, we also present the impact of temperature on the ICD-electron spectrum. Finally, our studies are complemented by comparing the directly computed KER spectrum to the mirror image of the ICD-electron spectrum, which coincide under certain conditions.

DOI: 10.1103/PhysRevA.107.023109

I. INTRODUCTION

Interatomic or intermolecular Coulombic decay (ICD) was originally predicted in 1997 [1] as a highly efficient electronic energy transfer mechanism in weakly bound systems, where after inner-valence ionization in one atom or molecule, the initial vacancy is filled by an outer-valence electron from the same system and the excess energy is radiationlessly transferred to a neighboring atom or molecule, resulting in its ionization. After the ICD process, two ions with outer-valence vacancies are thus formed. As they repel each other, the system usually disintegrates in a Coulomb explosion. A few years after its theoretical prediction, ICD was experimentally confirmed in neon dimers and clusters [2–4]. Since then, the process has been intensively studied in a variety of systems, establishing ICD as an important relaxation pathway in atomic and molecular clusters; see Refs. [5–8]. ICD was investigated in weakly bound systems, like the He dimer [9,10] and other van der Waals clusters like, e.g., Ne_n and NeAr [2,3,11,12], hydrogen-bonded clusters of H_2O and HF molecules [1,13–15], biologically relevant systems [16–18], as well as in liquids [19,20], quantum dots [21,22], and cavities [23]. Additionally, ICD inspired the investigations of further related mechanisms, such as ICD from electronic to vibrational states [24], double ionization by ICD (dICD) [25–28], ICD after Auger decay [29–34], electron-transfer-mediated decay (ETMD) [34–39], and interatomic Coulomb electron capture (ICEC) [40,41]. It was also demonstrated that the process can be initiated by ion [42] and electron impact [43–45].

The lifetime of an inner-valence ionized or excited state, which undergoes ICD, is of the order of femtoseconds. Although the nuclear motion of the involved monomers is usually slower, it has an impact on the ICD process, and therefore nuclear dynamics have to be taken into account when ICD is investigated. The coherent population of vibrational states, their broadening due to the partial decay widths, and the quantum superposition in their decay give rise to interference effects, which have to be considered as well. Experimentally and thus also theoretically preferred systems for such studies are noble gas dimers as the homoatomic Ne_2 [3,11,46–48] and He_2 [9,10,49], as well as the heteroatomic NeAr [50] and NeKr [51], where the nuclear dynamics in the ICD-electron and kinetic energy release (KER) ionic spectra were investigated.

Recently, the nuclear dynamics during ICD initiated by Ne2*s* ionization of a NeKr dimer were tracked experimentally [51]. The ICD in the NeKr dimer proceeds as follows. After ionization of the Ne, the 2*s* vacancy is filled by a 2*p* electron and the excess energy is transferred to the Kr, ejecting one of its 4*p* electrons. The two cations left behind repel each other and drift apart, which leads to a Coulomb explosion of the dimer. In brief, the process can be written as

$$\begin{aligned} \mathrm{NeKr} &\xrightarrow{\hbar\omega} \mathrm{Ne}^+(2s^{-1})\mathrm{Kr} + e^-_{\mathrm{PE}} \\ &\xrightarrow{\mathrm{ICD}} \mathrm{Ne}^+(2p^{-1}) + \mathrm{Kr}^+(4p^{-1}) + e^-_{\mathrm{PE}} + e^-_{\mathrm{ICD}}. \end{aligned} \quad (1)$$

*jacqueline.fedyk@pci.uni-heidelberg.de

The measuring method applied in Ref. [51] was based on the postcollision interaction technique [52,53], using the deceleration of the slow photoelectron e^-_{PE} when it gets overtaken by the fast ICD-electron e^-_{ICD}. The two singly-charged cations and the electron produced in the ICD process, as well as the photoelectron, were detected in coincidence using a COLTRIMS reaction microscope [54]. Time-resolved photoelectron (PE) and KER spectra, as well as survival probabilities of the decaying state, were measured and compared to theoretical simulations, which gave insight into the evolution of the vibrational wave packet during the ICD process. Although a good agreement between the theoretical and experimental spectra was obtained, the theoretical methodology used in Ref. [51] did not account for the interference effects in the PE and ICD spectra.

In the present work, we concentrate on the interference effects during ICD in NeKr and how they appear in the spectra of emitted particles. Although related, the sources of interference effects are different in the PE, ICD-electron, and KER spectra and reflect different aspects of the decay dynamics. As the decay width of the $Ne^+(2s^{-1})Kr$ state depends on the distance between neon and krypton, the photoelectron spectrum is not simply a sum of Lorentzians [55], reflecting the decay width of every populated vibrational state of the cation but contains an additional interference-like term [56]. Moreover, if the decay is fast, the broadening of the vibrational states, due to the partial decay widths, can be so large that the states overlap causing thus interference between the different channels. Finally, the wave-packet dynamics during the ICD process and the follow-up Coulomb explosion are additional sources of interference effects. The ICD-electron and KER spectra reflect the dynamics on the final and on the decaying state, respectively, where different portions of the wave packet can interfere with one another while propagating on the corresponding potentials.

Besides the interferences between the vibrational states, the PE spectrum is highly sensitive to changes in the potential energy curve (PEC) of the populated decaying state ($Ne^+(2s^{-1})$-Kr). This allows us to fine-tune the parameters of the corresponding PEC such that the computed PE spectrum reproduces best the experimental one. We also study the impact of isotope masses of neon and krypton on the spectra and motivated by the previous findings [47,50,57] allowing the selection of vibrationally excited states of the electronic ground state as an initial state, we computed vibrationally selected ICD-electron spectra for NeKr. The impact of the cluster temperature on the ICD-electron spectrum is also discussed. To complete our investigations, the KER spectra are directly calculated and compared to the mirror image of the corresponding vibrationally selected ICD-electron spectra.

II. THEORETICAL FRAMEWORK

In this section we briefly present the methodology used to describe the ICD process in NeKr and to compute the experimentally observable ICD-electron and KER spectra. Computational details regarding the numerical implementation of the working equations are also briefly discussed.

A convenient way to describe the dynamics of the process in Eq. (1) is the wave-packet propagation formulation of the electronic decay (see Refs. [58–60]). For this purpose, we first need to construct the potential energy curves (PECs) of all electronic states involved in the process and calculate the lifetime of the decaying state.

Initially, the NeKr dimer is in the electronic ground state $|\phi_i\rangle$. The corresponding PEC denoted as V_{gs} and shown in Fig. 1(a), was taken from Ref. [61]. It has its minimum at 3.63 Å and as can be seen in Fig. 1 supports five bound vibrational states.

Then the dimer is ionized leading to the population of the $Ne^+(2s^{-1})Kr$ state. We assume a broad-band ionization of Ne which is represented by a vertical transfer (red vertical arrow in Fig. 1) of the ground-state vibrational wave function of NeKr to the PEC V_d of the decaying state, which is shown in Fig. 1(d). The latter PEC was computed using the third-order algebraic diagrammatic construction scheme for approximating the one-particle Green's function [ADC(3)] [62,63], applying aug-cc-pCVQZ basis set on Ne and aug-cc-pVQZ basis set on Kr. The corresponding electronic state is denoted as $|\phi_d, E_{k_0}\rangle$, where $|\phi_d\rangle$ is the electronic wave function of the singly-ionized $Ne^+(2s^{-1})Kr$ dimer and $|E_{k_0}\rangle$ corresponds to the emitted photoelectron.

As the state is electronically unstable, its energy as a function of the internuclear distance is a complex number with an imaginary part being half of the decay width $\hat{\Gamma}_d$. The decay width [Fig. 1(c)] was computed with the Fano-ADC-Stieltjes approach [64], as described in Ref. [51]. The decaying-state PEC has 16 vibrational states, and each of them acquires a partial decay width Γ_{n_d}. Those widths are listed in Fig. 1(d). The minimum of the decaying-state PEC is located at 3.01 Å, i.e., slightly shifted to smaller internuclear distances compared to that of the ground-state PEC.

The decay width $\hat{\Gamma}_d$ of the decaying state determines the rate with which the population is transferred to the final electronic states $Ne^+(2p^{-1})Kr^+(4p^{-1})$. The latter states were computed with the second-order two-hole propagator ADC(2) method [65] using aug-cc-pVQZ basis sets on both atoms. In the range of internuclear distances relevant for the dynamics studied here, the PECs of the final states differ only slightly (see Fig. 1 of Ref. [51]). Consequently, the nuclear dynamics on the different final PECs are very similar and the resulting electron and KER spectra will be practically indistinguishable. For simplicity and clarity of the analysis, we thus used in the present study a single final PEC obtained as an average over all final states of interest. It is shown Fig. 1(b) and denoted as V_f. The final state is dissociative and at large internuclear distances, the corresponding PEC becomes purely Coulombic, as can be expected for two repelling cations, Ne^+ and Kr^+. The electronic final state can be written as $|\phi_f, E_{k_0}, E_{k_{\mathrm{ICD}}}\rangle$, where $|\phi_f\rangle$ gives the contribution of the repelling cations, $|E_{k_0}\rangle$ and $|E_{k_{\mathrm{ICD}}}\rangle$ correspond to the emitted photoelectron and the ICD electron $|E_{k_{\mathrm{ICD}}}\rangle$, respectively.

As already shown in Ref. [51], the PE spectrum is very sensitive to the form of the PEC of the decaying state V_d. We, therefore, first fitted this PEC by a Morse potential and then determined its parameters such that the computed spectra reproduce best the experimental ones.

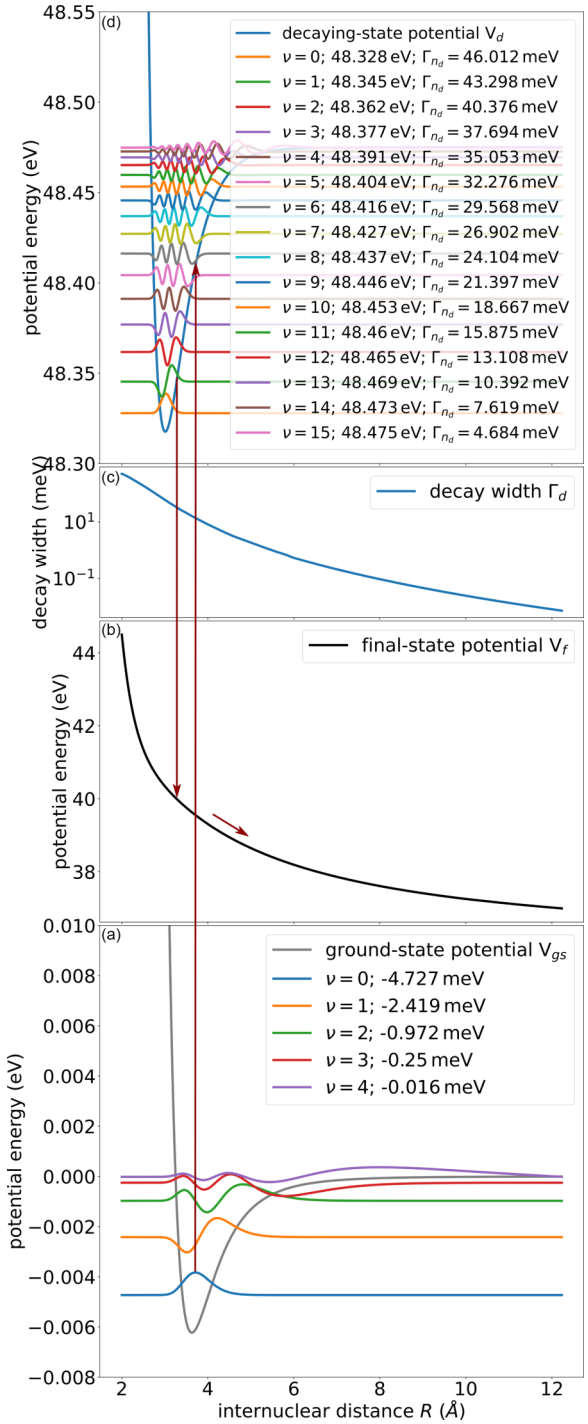

FIG. 1. PECs and decay width of the NeKr dimer and schematics of the ICD process. (a) The electronic ground state (V_{gs}) and its five vibrational states with the corresponding eigenenergies and eigenfunctions. By a broad-band ionization, the population is vertically transferred to the $Ne^+(2s^{-1})Kr$ electronic state (V_d), shown in panel (d), that decays by ICD and thus its potential has a complex contribution. The energies of the vibrational states and the corresponding decay widths are given in the legend. The total decay width is shown on a logarithmic scale in panel (c). The final ICD state $Ne^+(2p^{-1})Kr^+(4p^{-1})$, depicted in panel (b), is dissociative (V_f).

A. Photoelectron spectrum

The process of photoionization and the decay of the resulting ion can be described by the transition probability to go from an initial state $|I\rangle$ to a final state $|F\rangle$

$$P_{FI} = 2\pi\, |\langle F|\hat{\mathcal{T}}|I\rangle|^2\, \delta(E_I - E_F), \tag{2}$$

where $\hat{\mathcal{T}}$ is the transition operator, and E_I and E_F are the energies of the initial and final state, respectively. In the present case, the initial state $|I\rangle$ is the ground state of the NeKr dimer, which can be written as a product of the electronic state, the nuclear state, and the incoming photon $|\phi_i\rangle|n_i\rangle|\omega_p\rangle$. Consequently, the initial energy of the system equals the photon energy ω_p. The final state $|F\rangle$ is the repulsive dicationic state $Ne^+(2p^{-1})$-$Kr^+(4p^{-1})$, which can be written as a product of the electronic state, the nuclear state, the photoelectron, and the ICD electron $|\phi_f\rangle|E_{n_f}\rangle|E_{k_0}\rangle|E_{k_{\rm ICD}}\rangle$. Thus, the energy E_F includes the energies of the remaining cations and the two emitted electrons. Note that the vibrational states $|n_i\rangle$, $|n_d\rangle$, and $|E_{n_f}\rangle$ are eigenstates of the corresponding time-independent nuclear Hamiltonian, respectively.

The photoelectron spectrum can be derived from the transition probability by expanding the transition operator and by integrating over the final state $\int dE_{k_{\rm ICD}} \int dE_{n_f}$. By assuming a dipole transition and applying the local approximation [66–68], in which the decay width depends only on the internuclear distance and not on energy, one can obtain the PE spectrum. The local approximation typically works well when the decaying state is well above threshold, which in the present case is satisfied as the ICD process emits electrons of more than 8 eV. A detailed derivation of the expression for the PE spectrum can be found in Ref. [55]. The result reads

$$\sigma(\omega_b) = \langle n_i|\hat{V}^\dagger_{d\leftarrow i}(\omega_b - \hat{\mathcal{H}}^\dagger_d)^{-1}\hat{\Gamma}_d(\omega_b - \hat{\mathcal{H}}_d)^{-1}\hat{V}_{d\leftarrow i}|n_i\rangle. \tag{3}$$

The electronic states are included in the dipole matrix element $\hat{V}_{d\leftarrow i} = \langle\phi_d, E_{k_0}|\hat{D}|\phi_i\rangle$, ω_b is the binding energy, which equals the photon energy minus the kinetic energy of the photoelectron, $\omega_b = \omega_p - E_{k_0}$, and $\hat{\mathcal{H}}_d$ is the effective Hamiltonian of the decaying state in local approximation

$$\hat{\mathcal{H}}_d = \hat{H}_d - i\frac{\hat{\Gamma}_d}{2}, \tag{4}$$

where the real Hamiltonian $\hat{H}_d$ describes the nuclear motion in the decaying state, and the imaginary part contains the total decay width $\hat{\Gamma}_d$. Due to the decay, the energies of the vibrational states are shifted by Δ_d, which is incorporated into the real Hamiltonian $\hat{H}_d$. For further details about the energy shift and the derivation of the decay width within the local approximation, see Ref. [55].

The time-independent nuclear Schrödinger equation of the decaying state becomes

$$\hat{\mathcal{H}}_d|n_d) = \varepsilon_{n_d}|n_d), \tag{5}$$

where $\hat{\mathcal{H}}_d$ is a complex symmetric non-Hermitian Hamiltonian and its eigenvalues ε_{n_d} and eigenstates $|n_d)$ are both complex [69]. The complex nuclear eigenstates $|n_d)$ are usually written in round brackets to denote that they are differently normalized. As the left and the right eigenvector of a complex symmetric matrix are not adjoints but just transposed of each other, the orthogonality relation is now a c-product,

$(n_d|n'_d) = \langle n^*_d|n'_d\rangle = \delta_{n_d,n'_d}$ and the resolution of identity reads $\sum_{n_d}|n_d)(n_d| = 1$ (for a detailed discussion, see Ref. [69]). The corresponding eigenvalues are given by

$$\varepsilon_{n_d} = e_{n_d} - i\frac{\Gamma_{n_d}}{2}, \tag{6}$$

where Γ_{n_d} is the partial decay width of the vibrational state $|n_d\rangle$ and can be understood as a broadening of the energy level e_{n_d}, which consists of a small energy shift Δ_{n_d} and the solution of the time-independent Schrödinger equation of the real part of the Hamiltonian of the decaying state E_{n_d}. The corresponding Schrödinger equation of the real Hamiltonian reads

$$\hat{H}_d|n_d\rangle = E_{n_d}|n_d\rangle. \tag{7}$$

The final expression for the PE spectrum, which takes interference effects into account, is taken from Ref. [56] and reads

$$\sigma_{PE}(\omega_b) = \sum_{n_d}\frac{|\langle n_i|\hat{V}^\dagger_{d\leftarrow i}|n^*_d)|^2(n^*_d|\hat{\Gamma}_d|n_d)}{\left(\omega_b - E_{n_d}\right)^2 + \left(\Gamma_{n_d}/2\right)^2} + 2\mathrm{Re}\sum_{n_d>n'_d}\frac{\langle n_i|\hat{V}^\dagger_{d\leftarrow i}|n^*_d)(n^*_d|\hat{\Gamma}_d|n'_d)(n'_d|\hat{V}_{d\leftarrow i}|n_i\rangle}{\left(\omega_b - \varepsilon^*_{n_d}\right)\left(\omega_b - \varepsilon_{n'_d}\right)}, \tag{8}$$

where the first sum describes the PE spectrum without interference effects, while the second sum is associated with the interferences. The first sum alone is the standard formula for the PE spectrum, and we refer to it in the following as the standard PE spectrum equation.

Once we know the eigenvalues and eigenvectors of the ground and the decaying state, the implementation of our working equation Eq. (8) is straightforward. The Hamiltonian matrix can be written in discrete variable presentation (DVR) (see Ref. [70]) and then diagonalized. As noted above, for the non-Hermitian Hamiltonian of the decaying state, the complex eigenvectors have to be normalized according to the c-product relation; see also Ref. [69].

B. Interatomic Coulombic decay electron spectrum and kinetic energy release spectrum

For the computation of the ICD and KER spectra, we use the time-dependent formalism of wave-packet dynamics for the case of electronic decay (see, e.g., Refs. [58–60,71]). Within this approach, the nuclear dynamics of the ICD process can be described by wave packets propagating on the PECs involved. The total wave function can thus be written as a sum of all time-dependent states involved:

$$|\Psi(t)\rangle = |\phi_i\rangle|\psi_i(t)\rangle + \int_0^\infty dE_{k_0}\left|\phi_d, E_{k_0}\right\rangle\left|\psi_d\left(E_{k_0}, t\right)\right\rangle + \int_0^\infty dE_{k_0}\int_0^\infty dE_{k_{\mathrm{ICD}}}\left|\phi_f, E_{k_0}, E_{k_{\mathrm{ICD}}}\right\rangle \times \left|\psi_f\left(E_{k_0}, E_{k_{\mathrm{ICD}}}, t\right)\right\rangle, \tag{9}$$

where the $|\phi\rangle$'s are the corresponding electronic states and $|\psi(t)\rangle$'s are the nuclear wave packets propagating in the respective potentials. Because the decaying and the final states are associated with one and two electrons in the continuum, respectively, one has to integrate the energies of these electrons.

Before we continue, we briefly mention that the time-dependent nuclear wave functions can be expanded in a set of time-independent eigenfunctions,

$$|\psi_d(t)\rangle = \sum_{n_d} c_{n_d}(t)|n_d), \tag{10a}$$

$$\left|\psi_f\left(E_{k_{\mathrm{ICD}}}, t\right)\right\rangle = \int_0^\infty dE_{n_f} c_{E_{n_f}}\left(E_{k_{\mathrm{ICD}}}, t\right)\left|E_{n_f}\right\rangle, \tag{10b}$$

where $|n_d)$ and $|E_{n_f}\rangle$ are the eigenstates of the time-independent nuclear Hamiltonians $\hat{\mathcal{H}}_d$ and $\hat{H}_f$, respectively. $c_{n_d}(t)$ and $c_{E_{n_f}}(E_{k_{\mathrm{ICD}}}, t)$ are the corresponding expansion coefficients.

Returning to Eqs. (9), applying the weak field approximation, which forbids the back transfer of population from the decaying state to the initial state, assuming a broad-band (vertical) excitation, using the local approximation, and introducing dressed states to remove the photoelectron energy E_{k_0} [60], brings the time-dependent Schrödinger equation for the total wave function, Eq. (9), into a set of coupled differential equations for the nuclear wave functions evolving on the decaying and final state, respectively,

$$i|\dot{\psi}_d(t)\rangle = \hat{\mathcal{H}}_d|\psi_d(t)\rangle, \tag{11a}$$

$$i\left|\dot{\psi}_f\left(E_{k_{\mathrm{ICD}}}, t\right)\right\rangle = \hat{W}_{f\leftarrow d}|\psi_d(t)\rangle + \left(\hat{H}_f + E_{k_{\mathrm{ICD}}}\right)\left|\psi_f\left(E_{k_{\mathrm{ICD}}}, t\right)\right\rangle. \tag{11b}$$

The Hamiltonians $\hat{H}_d$ and $\hat{H}_f$ are associated with the nuclear motion in the corresponding electronic potential and are consequently given by $\hat{H}_{d/f} = \hat{T}_{\mathrm{nuc}} + \hat{V}_{d/f}$. $\hat{T}_{\mathrm{nuc}}$ is the kinetic energy operator of the nuclei and $\hat{V}_{d/f} = \langle\phi_{d/f}|\hat{H}_{el}|\phi_{d/f}\rangle + \hat{V}_{\mathrm{nuc}}$ is the corresponding PEC, where $\hat{H}_{el}$ is the electronic Hamiltonian and $\hat{V}_{\mathrm{nuc}}$ the nuclear repulsion.

The nuclear wave-packet dynamics in the final state consist of two contributions. The first is given by $\hat{W}_{f\leftarrow d}|\psi_d(t)\rangle$, which describes the transfer of population from the decaying state to the final state. The transition operator is defined as $\hat{W}_{f\leftarrow d} = \langle\phi_f, E_{k_{\mathrm{ICD}}}|\hat{H}_{el}|\phi_d\rangle$ and within the local approximation becomes energy-independent potential-like operator, closely related to the decay width: $\hat{\Gamma}(R) = 2\pi|\hat{W}_{f\leftarrow d}(R)|^2 = 2\pi\hat{W}^\dagger_{f\leftarrow d}\hat{W}_{f\leftarrow d} = 2\pi\hat{W}_{d\leftarrow f}\hat{W}_{f\leftarrow d}$. The second contribution to the final state dynamics is given by $(\hat{H}_f + E_{k_{\mathrm{ICD}}})|\psi(E_{k_{\mathrm{ICD}}}, t)\rangle$ and describes the propagation of the wave packet on the final PEC. These two contributions to the final-state wave packet can interfere. As the population transfer is continuous, the portion of the wave packet that is transferred from the decaying state at a given time can interfere with the portion that has been transferred at an earlier time and is already propagating on the final state. These interference effects can, of course, appear in the measured ICD-electron spectra.

These spectra can be computed from the solutions of Eqs. (11), as follows (see Refs. [58–60,71] for a detailed derivation):

$$\sigma_{\mathrm{ICD}}\left(E_{k_{\mathrm{ICD}}}\right) = \lim_{t\to\infty}\left\langle\psi_f\left(E_{k_{\mathrm{ICD}}}, t\right)\middle|\psi_f\left(E_{k_{\mathrm{ICD}}}, t\right)\right\rangle, \tag{12a}$$

$$\sigma_{\mathrm{KER}}(E_{\mathrm{KER}}) = 2\pi \int_0^\infty dt' \left| \langle E_{n_f} | \hat{W}_{f\leftarrow d} | \psi_d(t') \rangle \right|^2. \quad (12b)$$

As can be seen from Eq. (12), the ICD-electron spectrum is given by the population of the final state accumulated at infinite times, while the KER spectrum can be interpreted as the accumulated Franck-Condon factors between the decaying and the final state. The relation between the eigenenergies of the final state E_{n_f} and the kinetic energy release is given by $E_{\mathrm{KER}} = E_{n_f} - V_f^\infty$.

The time-dependent Schrödinger equations, Eqs. 11, were solved by using the MCTDH package [72,73]. In particular, we used the complex short iterative Lanczos integrator. To ensure that the wave packet propagating on the final state does not reach the end of the grid before the end of the process, a complex absorbing potential (CAP) [74,75] was introduced. The CAP is located on an interval at the end of the grid and, as the name suggests, has the function to absorb the incoming wave packet and in this way avoid its artificial reflection. Moreover, the CAP and more precisely the flux going through it can be directly used to compute the ICD-electron spectrum, provided the entire wave packet propagating on the final potentials has been absorbed. For a detailed explanation regarding the MCTDH method and program, and in particular, the flux analysis and the application of CAPs, see Ref. [73].

III. INTERFERENCE EFFECTS IN THE PHOTOELECTRON SPECTRUM

As we discussed already, the population of the decaying state is performed by the removal of Ne2*s* electron from the NeKr dimer. This can be done by photoionization and as the populated state is a decaying one, it is intuitively clear that the photoelectron carries also information on the decay. Therefore, the photoelectron spectrum will contain not only the total decay width of the decaying electronic state but also information on its vibrational structure and partial decay widths, i.e., on the subsequent decay dynamics. In this section, we will discuss the photoelectron spectrum, focusing on the interference effects which can occur and get imprinted within it. The interferences arise due to the different partial decay widths of the coherently populated vibrational states of the decaying state [56]. The different decay widths, in turn, appear as a result of the dependence of the total decay width on the internuclear distance, $\Gamma = \Gamma(R)$. If Γ is constant, every vibrational state will have the same decay width and the PE spectrum will be given by the standard formula, i.e., a sum of Lorentzians, one for every populated vibrational state, weighted by the corresponding Franck-Condon factors. Moreover, the decay width can be larger than the energy spacing between the vibrational states, and therefore the populated states will overlap in energy causing an additional interference effect.

In general, the PE spectrum is highly sensitive to the shape of the PEC of the decaying state and the respective partial decay widths. Before we start our investigation of the interference effects in the PE spectrum, we want to make sure that the computed spectra reproduce well the measured ones, reported in Ref. [51]. Although the PECs have been obtained by the high-level *ab initio* method [ADC(3)], highly excited and moreover decaying states of weakly bound van der Waals clusters are very difficult to compute. Obtaining electronic decay widths, especially for interatomic processes, poses even larger difficulties. Discrepancies of 20% [76] and even larger [77] have been reported for decay widths obtained by Fano-ADC-Stieltjes method, used to compute the decay width of the $Ne^+(2s^{-1})Kr$ state. In addition, by comparing the experimental and theoretical survival probabilities it was already shown in Ref. [51] that *ab initio* decay width of $Ne^+(2s^{-1})Kr$ is overestimated. We, therefore, scaled the *ab initio* decay width by the constant factor of 0.8 (sc = 0.8), which gives the best agreement with the experimentally observed survival probability. We note that even after this rescaling, the follow-up ICD process is still ultrafast. The decay width at the equilibrium geometry is 16 meV, corresponding to a lifetime of about 41 fs. We can now use the experimental spectra and adjust the PEC of the decaying state assuming a scaled decay width.

We approximate the PEC of the decaying state with a Morse potential and as a starting guess fitted its parameters to the *ab initio* data. We, therefore, have

$$V_d(R) = D_e\,(1 - e^{-\alpha(R-R_e)})^2, \quad (13)$$

where D_e is the depth, R_e marks the equilibrium position, and α controls the width of the potential well. A grid search was then performed, where for each combination of parameters (D_e, R_e, and α), the PE spectrum was computed and compared to the experimental one. This procedure was repeated until the difference between computed and measured data became minimal. As mentioned in the introduction, the PCI technique was used in the experiment. The photon energy, therefore, was only slightly above the ionization threshold of 48.68 eV. This allows the later emitted fast ICD electron to overtake the slow photoelectron, which then gets decelerated due to the increased charge of the parent ion. This PCI effect appears as a tale in the low-energy part of the PE spectrum; see Appendix A. We do not take the PCI effects into account in our calculations and that is why we compare the computed PE spectrum only with the higher energy part of the experimental one. For a better comparison, we also convolve the computed spectra with a Gaussian with full width at half maximum (FWHM) of 30 meV to account for the reported experimental resolution of ±15 meV.

Due to the relatively simple PE spectrum, there are several parameter combinations that lead to a rather good agreement with the measured data. We, therefore, determined the Morse-potential parameters computing the KER spectrum and comparing it with the experimental one. Details for the impact of the Morse-potential shape on the PE and KER spectra are given in Appendix A. The parameters that give best agreement with experiment are therefore $D_e = 0.16$ eV, $R_e = 3.01$ eV, $\alpha = 1.09$ au^{-1}, and sc = 0.8. In the following, we refer to this PEC as working Morse potential.

The PE spectra computed with the working Morse potential, with and without interference effects are shown in Fig. 2 together with the higher energy part of the experimental result for a photon energy of 48.68 eV. We see that the PE spectrum, which takes interference effects into account (blue curve) agrees well with the experiment (blue dots) and that

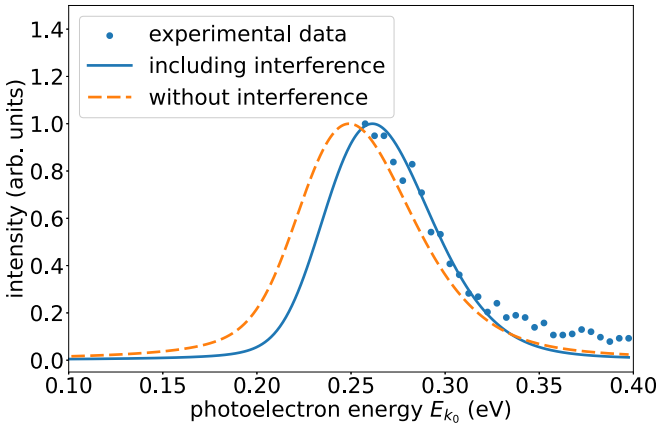

FIG. 2. Comparison of the photoelectron spectra computed with (solid curve) and without (dashed curve) interference effects and the experimental one (blue dots) reported in Ref. [51] for photon energy of 48.68 eV. The spectra are normalized to their maximum intensity.

the standard PE spectrum has a similar form, but is slightly shifted to lower energies.

Before analyzing in more detail the interference effects in the PE spectrum, we would like to note that the spectra presented in Fig. 2 are obtained by computing a spectrum for each isotope mass combination and then summing up these PE spectra which are weighted by the natural abundance of the respective isotope composition. The impact of isotope mass on the PE spectrum can be found in Appendix B. For our theoretical study in the following, we use the isotopic mass combination that most frequently occurs in nature, namely a reduced mass of 16.15 AMU.

To better understand the impact of the interference effects on the PE spectrum, Fig. 3 shows the full computed spectrum [Eq. (8)] and its individual contributions, which are the standard PE spectrum [first sum in Eq. (8)], and the interference term [second sum in Eq. (8)]. As seen in Fig. 3, the contribution of the interference term is negative and thus

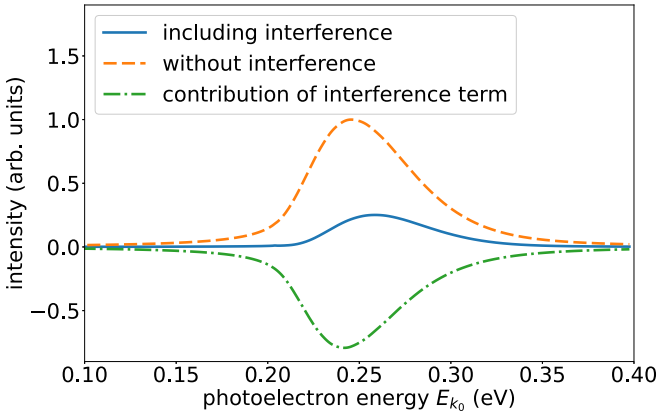

FIG. 3. Computed PE spectra with (solid curve) and without (dashed curve) interference effects, and the isolated contribution of the interference term (dash-dotted curve). The spectra are computed for a dimer with a reduced mass of 16.15 AMU (the most frequently occurring isotope mass combination) assuming that before ionization the system is in its vibrational ground state $\nu = 0$.

associated with a destructive interference. Both terms have nearly opposite behavior as a function of the photon energy and the result is that the total PE spectrum is slightly shifted to higher photoelectron energies compared to the standard spectrum. In the present case, the interference effects are a combination of the coherent population of vibrational states with different partial decay widths (R dependence of Γ) and their overlap in energy due to the large partial decay widths and the small energy difference between the states (shallow potential).

Since Γ gets smaller at larger internuclear distances, the higher-lying vibrational states have a smaller partial decay width. This favors the contribution of the lower-lying vibrational states in the PE spectrum. In the present case, the R-dependence is very monotonic (at large internuclear distances $\Gamma \sim R^{-6}$ [78]) making that the interference term causes mostly a shift in the PE spectrum. A more involved dependence of the decay width on the internal degrees of freedom of the system can lead to a more dramatic effect of the interference term in the PE spectrum.

The large total decay width and the small energy spacing between the vibrational states also affect the contribution of the interference. Smaller partial decay widths, or less overlapping vibrational states, will lead to a more structured PE spectrum, where each populated vibrational state gives one peak in the spectrum, but also smaller interference effects, at least when Γ monotonically decreases. In situations where the decay width has a complicated functional dependence on the system geometry and combinations of overlapping and nonoverlapping vibrational states are populated, accounting for the interference effects can be crucial for understanding the PE spectrum.

IV. VIBRATIONALLY SELECTED INTERATOMIC COULOMBIC DECAY

Let us now continue our study with the analysis of the ICD-electron spectrum. After the photoionization, the populated $Ne^+(2s^{-1})Kr$ state decays by ICD, emitting an electron. The spectrum of emitted ICD-electron was obtained using the methodology outlined in Sec. II B and Eq. (12). The ICD process assuming that the NeKr dimer is initially in its vibrational ground state was studied already in Ref. [51]. Therefore, here we will concentrate mostly on vibrationally selected ICD. We will investigate the process, assuming that the whole population is initially in one vibrationally excited state of the electronic ground state. This will also allow us to study the effect of the temperature of the cluster on the ICD-electron spectrum.

As already discussed in Sec. II and shown in Fig. 4, the electronic ground state of NeKr supports five bound vibrational states. The ICD-electron spectra that will be produced by a broad-band ionization starting from each of these states are shown in Fig. 4. We see that by going up in the ground-state vibrational progression, the ICD-electron spectrum moves to higher energies. The vibrationally selected ICD, therefore, offers control over the kinetic energy of the emitted ICD electron.

As the ICD is very fast, the wave packet created on the decaying state has practically no time to evolve on V_d potential

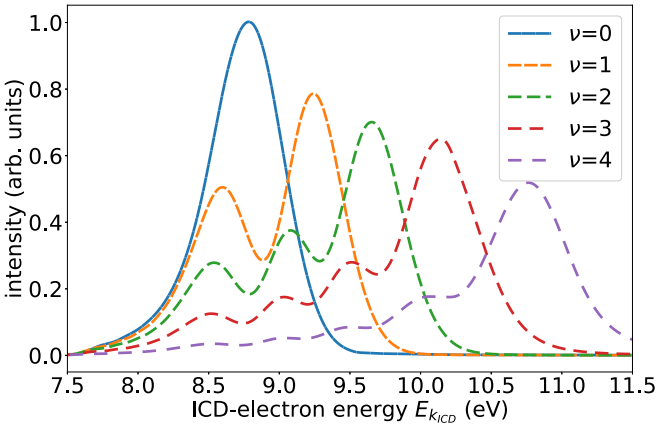

FIG. 4. Computed vibrationally selected ICD-electron spectra. The spectra are calculated assuming that before the photoionization the system is in one of the five vibrational levels of the electronic ground state, $\nu = 0$ to 4.

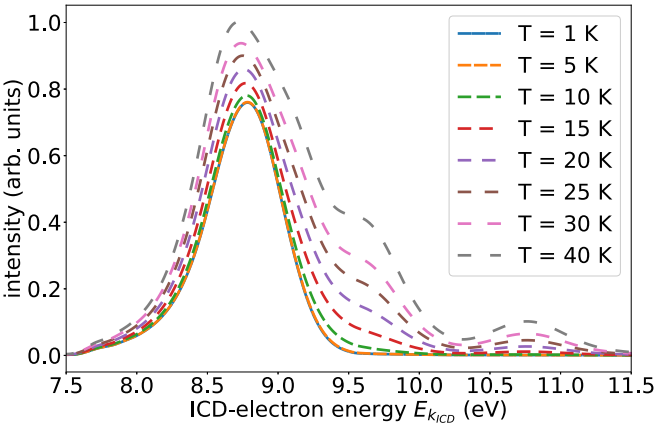

FIG. 6. Computed ICD-electron spectra of NeKr at different temperatures.

and is nearly immediately transferred to the final state. This makes the ICD-electron spectrum practically a direct image of the population of the initial vibrational state. This can be confirmed by comparing the spectra shown in Fig. 4 with the probability densities, or the modulus square of the respective vibrational wave functions, shown in Fig. 5. As we see, the vibrationally selected ICD-electron spectra clearly reflect the nodal structure of the corresponding initial vibrational wave function.

Let us now return to the main focus of our study, the role of the interference effects in the process. As noted in Sec. III, interferences can result both from the decaying and the final states. Of course, the interference effects on the decaying state always indirectly affect the propagation of the wave packet on the final state. Even without final-state interferences, the ICD-electron spectrum would not simply be the inverse population of the decaying state, because the energy between decaying and final state is not well defined due to the decay width $\hat{\Gamma}_d$. The ICD-electron spectrum, however, reflects the nuclear dynamics on the final state, because it is given by the population of the final state accumulated over time; see

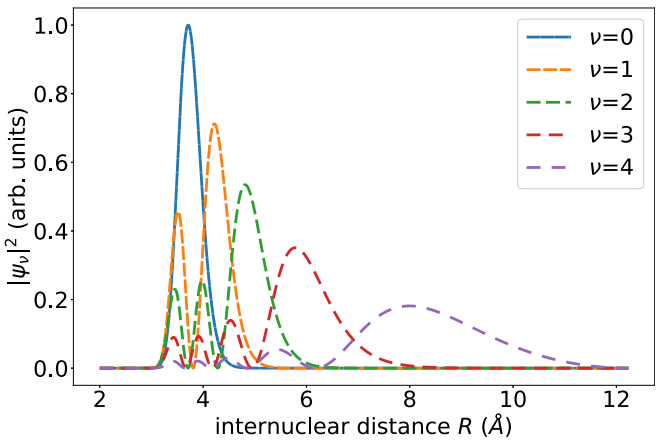

FIG. 5. Probability densities $|\psi_\nu|^2$ of all five bound vibrational states of the electronic ground state of NeKr.

Eq. (12 a). The interference effects on the final state occur due to the continuous transfer of population from the decaying to the final state which means that portions of the wave packet arriving at later times can interfere with portions of the wave packet already propagating on the final state. Clearly, these effects can lead to noticeable modifications of the spectra if the decay is somewhat slower and gives time for the evolution of the wave packet both on the decaying and on the final state.

Depending on the way of their preparation (usually by supersonic coexpansion), the rare gas clusters may have a different temperature. The vibrationally selected ICD provides the possibility to analyze the dependence of the spectra on the temperature. It is usually assumed that before ionization the dimer is in its vibrational ground state, which is certainly the case at $T = 0$ K. At higher temperatures, however, the population gets statistically distributed to higher-lying vibrational states. We can, therefore, introduce the impact of temperature in our computations by weighting the vibrationally selected ICD-electron spectra by the Boltzmann distribution $w_\nu = e^{-\beta E_\nu}$, where $\beta = (k_B T)^{-1}$ with k_B being the Boltzmann constant, and then summing them up incoherently. The ICD-electron spectra at different temperatures are given in Fig. 6.

We see that a slight difference in the spectrum appears already at 10 K, which is the estimated temperature of the dimers in the experiment reported in Ref. [51], but this increase in intensity at about 9.5 eV is too small to be experimentally resolvable. More noticeable differences start to appear at temperatures higher than 20 K, where the main peak develops a clear shoulder and a second peak at 10.8 eV starts to appear. We can, therefore, conclude that for the NeKr dimer the approximation that only the vibrational ground state is initially populated is valid for temperatures of up to about 20 K. This corresponds to population rates of the vibrationally excited states of 26% for the first vibrationally excited one, and still over 11% and 7% for the second and third one. In comparison, at 10 K only 7% of the population is in the first excited vibrational state, and only 1% in the second one.

We would like to conclude our study by examining the KER spectrum of the Coulomb exploding dimer, again concentrating on the interference effects and how they are imprinted within it.

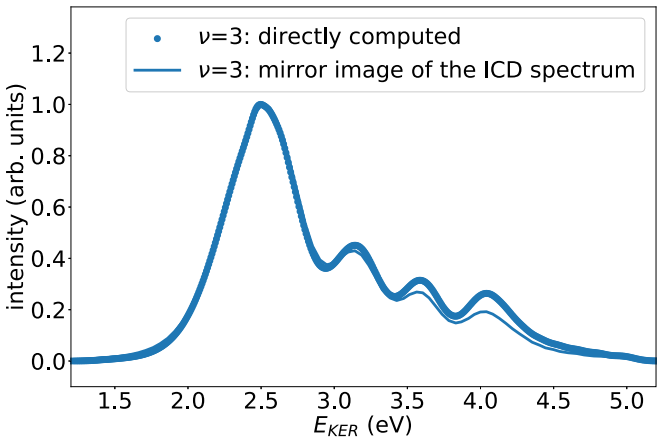

FIG. 7. Directly computed KER spectrum (dots) and the mirror image of the ICD-electron spectrum (solid line). The population is initially assumed to be in the third vibrationally excited state $\nu = 3$ of the electronic ground state. The spectra are scaled by the highest value of the spectrum.

While the ICD-electron spectrum records the propagation on the final state, the KER spectrum reflects the nuclear dynamics in the decaying state. As seen from Eq. (11b), it is related to the projection of the decaying-state wave packet on the final state. Therefore, the ICD and KER spectra carry complementary information [71]. In the classical picture, however, the KER and the ICD-electron spectra are mirror images of each other (mirror-image approximation). Although this is often used in practice, it was shown [60,71] that due to the quantum effects, the mirror-image principle breaks down and is a good approximation only in cases of a small decay width and no or negligible nuclear dynamics on the decaying state. Due to the very shallow V_d potential, the dynamics in the decaying state of NeKr are not fast. However, the decay width is rather large, leading to interference effects in the PE spectrum. Can such an intermediate situation lead to noticeable deviations from the mirror image approximation?

The KER spectra directly computed by Eq. (12 b) following a vibrationally selected ICD process, as well as KER spectra at various temperatures, can be found in Appendix C. The results show that the directly computed KER spectrum and the mirror image of the ICD-electron spectrum agree well, at least if only the vibrational ground state is initially populated. Comparing the KER spectrum and the mirror image of the ICD-electron spectrum corresponding to the higher vibrationally excited states, however, show discrepancies at higher KER energies. An example of an ICD process initiated from the third excited vibrational state of the ground state is shown in Fig. 7. The mirror image of the ICD-electron spectrum is lower in intensity than the directly computed KER spectrum and the deviation increases with energy, which implies destructive interference.

While in the KER spectrum, only the dynamics and the corresponding interference effects in the decaying state are tracked, the ICD-electron spectrum carries more information. It gives insight into the wave-packet motion in the final state, which also depends on the dynamics in the decaying state; see Eqs. (11). The propagation in the final state is accompanied by leakages from the decaying state that interfere with the final-state wave packet. Because the KER spectrum does not display these final-state interferences, we may conclude that they need to be small to guarantee that the mirror image is a good approximation.

In the case of the initially populated vibrational ground state, this is guaranteed by the large decay width. Due to the fast decay, the entire population of the decaying state is nearly immediately transferred to the final state leaving practically no time for the different portions of the wave packet to propagate and interfere in the final state. Returning to the vibrationally selected ICD in Fig. 7, we see the reason for the discrepancies between the mirror image and the directly computed KER spectrum. The third vibrationally excited state is more delocalized compared to the ground state and therefore, higher vibrational states of the decaying state are populated, which have smaller partial decay widths (the total decay width decreases with R). Therefore, for some parts of the wave packet, there is more time for propagation on the decaying, and consequently also on the final state, which leads to interferences. We can thus conclude that final-state interferences can be suppressed by a short lifetime of the decaying state and increased by somewhat longer decay times.

V. SUMMARY AND CONCLUSIONS

In our work, we investigated the ICD process in the NeKr dimer initiated by a Ne2s ionization, concentrating on the role of the interference effects in the ionization and subsequent decay. We also studied the vibrationally selected ICD process, in which the system is initially prepared in a vibrationally excited state of the electronic ground state of the neutral dimer, and showed that the interference effects can be even more pronounced in such cases. There are two different sources of interferences. Interferences can occur as a result of the coherent population of vibrational levels that overlap because they are differently broadened by the total decay width that depends on the internal degrees of freedom of the system, $\Gamma_d(R)$. But they can also arise from the nuclear dynamics in the final state, as different portions of the wave packet transferred to it during the decay can interfere with each other.

Interestingly, even the PE spectrum of the ionization populating the initial ICD state $[Ne^+(2s^{-1})Kr]$ is sensitive to the interference effects in the decaying state. The dependence of the total decay width on the internuclear distance accompanied by the overlapping of the vibrational levels due to the large partial decay widths lead to destructive interference that shifts the spectrum to larger energies compared to the standard PE spectrum computed without interference effects. Moreover, due to its strong dependence on the populated vibrational energy levels and the corresponding partial decay widths, the PE spectrum is very sensitive to the shape of the decaying state PEC. This can, therefore, be used to obtain satisfactory PECs of decaying states, especially when the decay width strongly depends on the internal degrees of freedom, like in the case of ICD. It should be noted, however, that very often additional spectroscopic data, reflecting the dynamics on the decaying state, may be needed. In the present case, such additional information could be extracted from the experimental KER spectrum. This allowed us to construct a satisfactory PEC

of the $Ne^+(2s^{-1})Kr$ state by optimizing the parameters of a Morse potential that best reproduce the experimental spectra.

We also performed full dynamics simulations of the ICD processes following Ne2*s* ionization and computed vibrationally selected ICD spectra. In the vibrationally selected ICD processes, the population is initially in one of the vibrational levels of the electronic ground state. As the ICD process is very fast [the lifetime of $Ne^+(2s^{-1})Kr$ is about 50 fs], the wave packet has practically no time to propagate on the decaying-state potential and the vibrationally selected ICD-electron spectra image the wave functions of each initial vibrational state. The vibrationally selected ICD spectra can be also used to assess the effect of temperature. Our calculations show that already at 10 K slight differences in the spectra start to appear and at 20 K the spectra already show two additional peaks.

Another possibility to study ICD in NeKr is to analyze the distribution of the kinetic energy release of the produced Ne^+ and Kr^+ ions after the decay. The KER and the ICD-electron spectra provide actually complementary information. While the KER spectrum reflects the nuclear dynamics in the decaying state, the ICD-electron spectrum exhibits the nuclear dynamics in the final state. The two spectra, therefore, record different interference effects. Consequently, they are not exactly a mirror image of each other, although this approximation is used very often. In cases when the interference effects in the decaying and the final states are strong, the two spectra can show substantial differences. In the present case, due to the large decay width, the interference effects in the final state are rather small, as the wave packet gets transferred very fast from the decaying state, and ICD-electron and KER spectra from the vibrational ground state are nearly a perfect mirror image to each other. However, if the photoionization is performed from an excited vibrational state, the KER and ICD-electron spectra start to differ at higher KER energies.

In the end, we would like to note that the present study shows that vibrationally selected ICD processes give access to a wealth of information on the quantum dynamics of the decaying system, and we hope that our work will motivate not only further theoretical, but also experimental studies of these ICD processes in other systems.

ACKNOWLEDGMENTS

We would like to thank F. Trinter for providing us the experimental data. Financial support by the European Research Council (ERC) (Advanced Investigator Grant No. 692657) is gratefully acknowledged.

APPENDIX A: MORSE FIT

As explained in Sec. III, a Morse potential is fitted to the *ab initio* PEC of the decaying state and its parameters are then adjusted such that the computed PE spectrum reproduces best the experimentally measured one. An important characteristic of this nonstationary state is its decay width $\Gamma(R)$, which was computed by the Fano-ADC-Stieltjes method, but was also optimized by comparing to the experimental PE spectrum. The best agreement we find with a Morse potential with parameters $D_e = 0.16$ eV, $R_e = 3.01$ eV, and $\alpha = 1.09$ au^{-1}, and a decay width scaled by 0.8. Due to the relatively simple form of the PE spectrum, there are different sets of parameters that provide a good agreement with experiment. Here we would like to discuss why we chose this set of parameters for our working Morse potential and how the different parameters influence the PE and ICD-electron spectra.

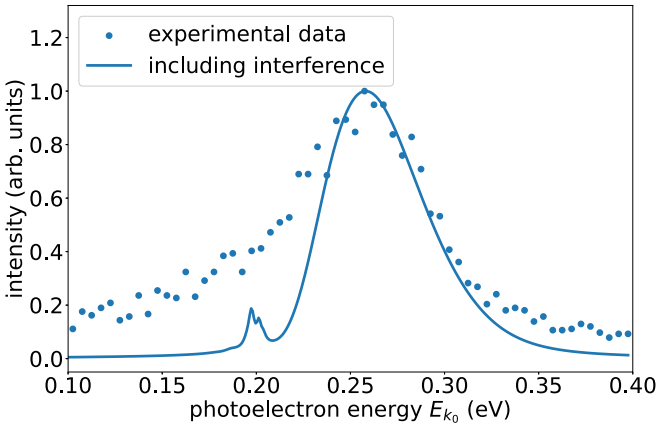

FIG. 8. Computed PE spectrum with interference effects and unscaled decay width (line) compared to experimentally measured PE spectrum taken from Ref. [51] (dots) for a photon energy of 48.68 eV.

Let us start with why it is necessary to scale the decay width. The Fano-ADC-Stieltjes method usually overestimates the decay width [76,77]. Due to the resulting large broadening of the vibrational energy levels, they greatly overlap, which leads to stronger interference effects. In Fig. 8 we show a comparison between a PE spectrum computed via Eq. (8) for our working Morse potential, but with an unscaled decay width. To better expound the effect of the larger decay width on the PE spectrum, we do not convolve it with a Gaussian to account for the experimental resolution. The spectrum is computed under the assumption that only the vibrational ground state is initially populated.

One can see that besides the main peak, which agrees well with the experiment, the computed PE spectrum exhibits an additional smaller peak at lower energies, which is not observed experimentally. We note that due to the PCI effect, the low-energy part of the experimental PE spectrum exhibits a smooth tail because the faster ICD electrons overtake the slower PE electrons, which are decelerated due to the missing shielding of the ICD electrons. As in our computations, we do not take the PCI effect into account, we use for the optimization of the decaying state PEC V_d only the higher-energy part of the experimental spectrum. Importantly, the small peak at 0.2 eV appears solely due to the interference effects, which are suppressed if the decay width is smaller. The peak disappears if we take only 80% of the originally computed decay width.

We now turn to the parameters determining the shape of the Morse potential. The results of the grid search highly depend on the initial guess and the given ranges for the parameters. For the PEC we finally use in this work, we define parameter search ranges maximally close to the Morse fit of the *ab initio* PEC. However, as explained above, several parameter combinations give good agreement between the theoretical and experimental PE spectra. In Fig. 9 we present a PE spectrum computed with a slightly shifted Morse potential with

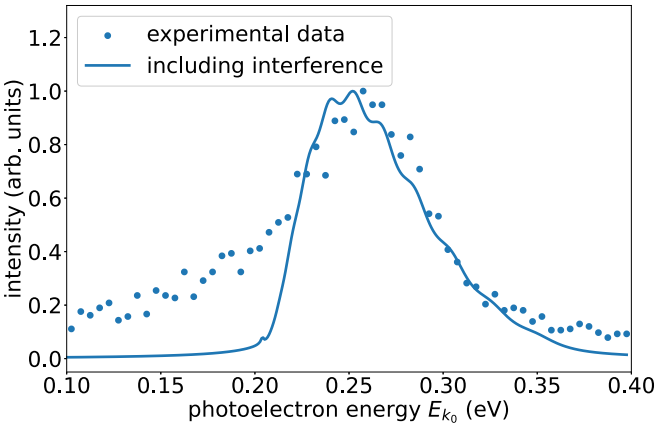

FIG. 9. Computed PE spectrum with interference effects (line) using the alternative Morse potential ($D_e = 0.16$ eV, $R_e = 3.18$ eV, $\alpha = 1.51$ au^{-1}, and sc $= 0.8$) compared to the experimentally measured PE spectrum taken from Ref. [51] (dots).

a narrower potential well, to which we refer in the following as alternative Morse potential ($D_e = 0.16$ eV, $R_e = 3.18$ eV, $\alpha = 1.51$ au^{-1}, and sc $= 0.8$).

Again, only the vibrational ground state of the neutral dimer is assumed to be initially populated and we do not convolute the resulting spectrum with a Gaussian. The spectrum shows more structure, which, however, cannot be resolved experimentally. The agreement between the computed and measured spectrum is even better for the alternative Morse potential than for the working Morse potential. The PE spectrum, however, reflects only the initial step of the dynamics triggered by the Ne2s ionization. The KER spectrum of the Coulomb explosion following the ICD process is also very sensitive to the decaying-state potential, as it actually reflects the nuclear dynamics in the $Ne^+(2s^{-1})Kr$ state [see Eq. (12 b)]. We, therefore, should take also the KER spectrum into account when determining the optimum parameters of the decaying-state Morse potential.

Figure 10 shows the KER spectrum computed with the alternative Morse potential compared to the experimental data

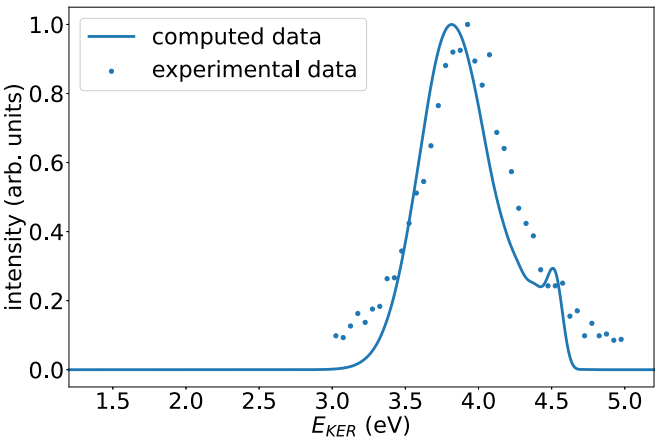

FIG. 10. Computed KER spectrum (line) for the alternative Morse potential ($D_e = 0.16$ eV, $R_e = 3.18$ eV, $\alpha = 1.51$ au^{-1}, and sc $= 0.8$) in comparison to the measured KER spectrum taken from Ref. [51] (dots).

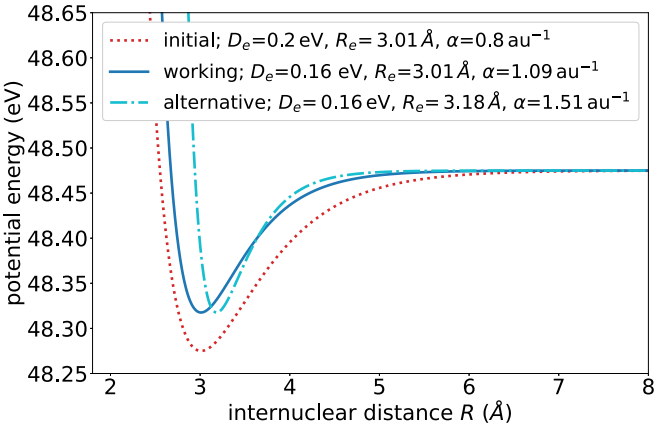

FIG. 11. Potential energy curves for the different Morse fits. The fit to the original *ab initio* potential (dotted curve), the working Morse potential (solid curve), and the alternative Morse potential (dash-dotted curve). The Morse potential is given by Eq. (13), and the corresponding parameters are listed in the legend.

taken from Ref. [51]. We see that there are substantial differences. The computed spectrum shows a structure at about 4.5 eV which is not observed experimentally. We can, therefore, conclude that the PE spectrum does not contain sufficient information to fully reconstruct the decaying state PEC. Other experimental observables such as the KER spectrum could be very useful in this case.

The different Morse potentials are shown in Fig. 11.

APPENDIX B: IMPACT OF ISOTOPE MASSES

In this Appendix, we analyze the impact of the nuclear mass on the PE spectrum. If only the vibrational ground state is initially populated, the effect of the different isotope masses on the PE spectrum is negligibly small. More interesting are the PE spectra obtained by ionizing already vibrationally excited neutral dimers (vibrationally selected PE spectrum). The results for the PE spectrum of a dimer being initially in its first excited vibrational state are shown in Fig. 12. The spectra corresponding to the lowest possible (reduced mass of 15.91 AMU), the highest possible (reduced mass 17.51 AMU), and the most frequently occurring (reduced mass 16.15 AMU) isotope-mass combinations are displayed. All spectra include interference effects and are normalized to their highest intensity value. We see that the spectra are markedly different, showing that the vibrationally selected PE spectrum can be sensitive to the isotope mass composition of the dimer.

This high sensitivity shows that for vibrationally selected PE spectra, the usual way to take the isotope effect into account, namely to average the reduced mass (being 16.26 AMU in the present case) might not be a good approximation. Instead, one needs to compute the spectrum for every isotope combination and average afterwards, weighting with the natural abundance of the corresponding isotopes. In Fig. 13 we compare the vibrationally selected ($\nu = 1$) PE spectra obtained by averaging the reduced mass (orange) and by averaging the weighted spectra of every mass combination (blue). We see that the two averaging procedures can lead to substantial differences in peak intensities and thus for the

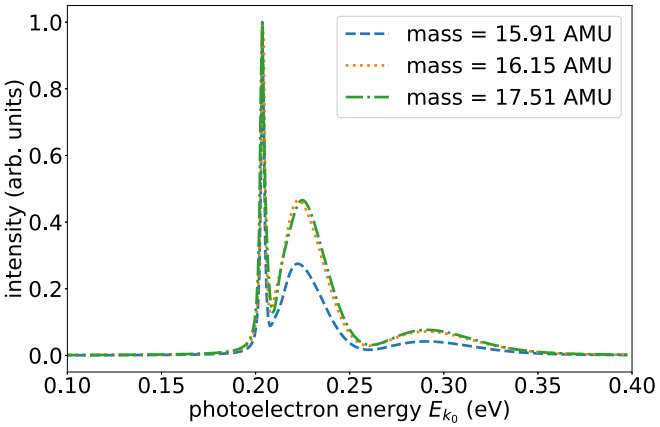

FIG. 12. Computed vibrationally selected ($\nu = 1$) PE spectra including interference effects for different isotope-mass combinations. The lowest (dashed curve), the highest (dash-dotted curve), and the most frequently occurring (dotted curve) isotope-mass combinations are shown. The corresponding reduced masses are given in the legend. Photon energy of 48.68 eV is assumed.

vibrationally selected ICD processes, we cannot use the averaged reduced mass to calculate the spectra. We, therefore, used in the present work the most frequently occurring isotope combination and its reduced mass of 16.15 AMU.

APPENDIX C: KINETIC ENERGY RELEASE SPECTRUM

After ICD has taken place, the NeKr dimer undergoes a Coulomb explosion, where the Ne and Kr ions fly apart. The KER spectrum gives the distribution of kinetic energies of the two cations. Thereby, the KER is the difference between the final-state potential at nuclear distances of the decay and at infinity, $E_{\mathrm{KER}} = E_{n_f} - V_f^{\infty}$. The KER spectrum, however, reflects the nuclear dynamics in the decaying state by projecting the wave packet propagating in the decaying state on the final state [see Eq. (12 b)]. No interference effects in the final state appear in the KER spectrum.

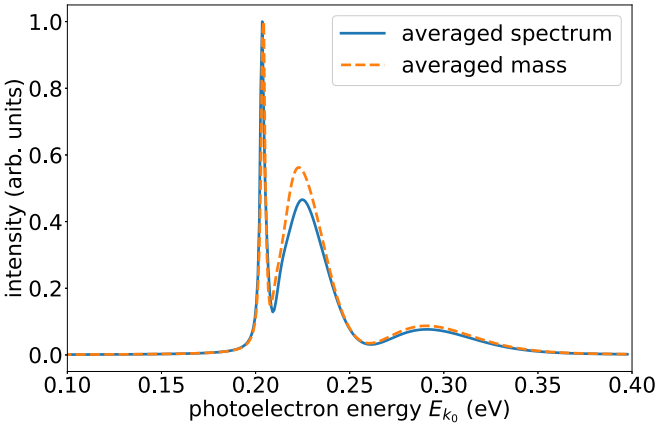

FIG. 13. Computed vibrationally selected ($\nu = 1$) PE spectra including interference effects, obtained by averaging the reduced mass (dashed curve) and by averaging the weighted spectra of every mass combination (solid curve). The averaged reduced mass used is 16.26 AMU. Photon energy of 48.68 eV is assumed.

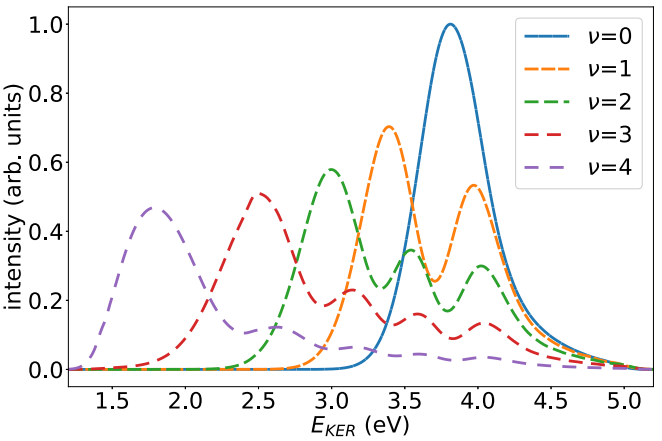

FIG. 14. Computed vibrationally selected KER spectra. The spectra are calculated assuming that before the photoionization the NeKr is in one of the five vibrational levels of the electronic ground state, $\nu = 0$ to 4. The most frequently occurring isotope-mass combination of 16.15 AMU (reduced mass) is used.

Here we report the KER spectra following a vibrationally selected ICD process, that is, the NeKr dimer is in one of the five vibrational levels of its ground electronic state at the moment of the photoionization. The resulting KER spectra are shown in Fig. 14.

The KER energies lie between 1.2 eV and 5.2 eV depending on the vibrationally selected channel and due to the ultrafast ICD process, the KER spectra reflect the initial vibrational wave functions and reproduce their nodal structures.

For completeness, we also report here the dependence of the KER spectra on the temperature of the NeKr dimer. Those are displayed in Fig. 15. As for the ICD-electron spectrum, a small impact of the temperature can be observed already at 10 K. The effect increases with the increase of temperature and becomes clearly visible at 20 K, where the processes initiated from the excited vibrational states start to contribute more substantially. New peaks at 1.75 eV and 3 eV appear at higher temperatures.

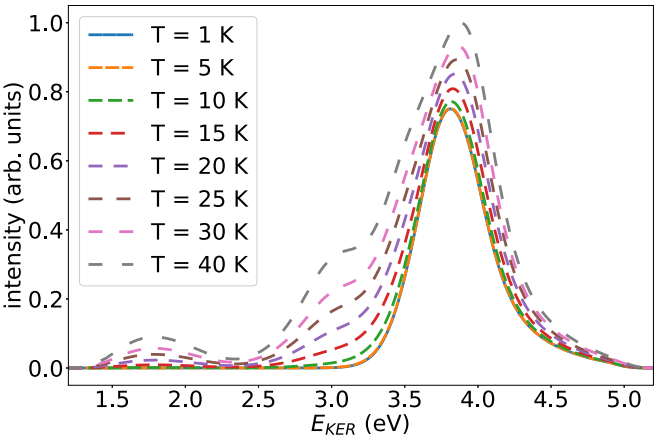

FIG. 15. Computed KER spectra at different temperatures. The most frequently occurring isotope-mass combination of 16.15 AMU (reduced mass) is taken.

[1] L. S. Cederbaum, J. Zobeley, and F. Tarantelli, Phys. Rev. Lett. **79**, 4778 (1997).

[2] S. Marburger, O. Kugeler, U. Hergenhahn, and T. Möller, Phys. Rev. Lett. **90**, 203401 (2003).

[3] T. Jahnke, A. Czasch, M. S. Schöffler, S. Schössler, A. Knapp, M. Käsz, J. Titze, C. Wimmer, K. Kreidi, R. E. Grisenti *et al.*, Phys. Rev. Lett. **93**, 163401 (2004).

[4] G. Öhrwall, M. Tchaplyguine, M. Lundwall, R. Feifel, H. Bergersen, T. Rander, A. Lindblad, J. Schulz, S. Peredkov, S. Barth *et al.*, Phys. Rev. Lett. **93**, 173401 (2004).

[5] V. Averbukh, P. Demekhin, P. Kolorenč, S. Scheit, S. Stoychev, A. Kuleff, Y.-C. Chiang, K. Gokhberg, S. Kopelke, N. Sisourat, and L. Cederbaum, J. Electron Spectrosc. Relat. Phenom. **183**, 36 (2011).

[6] U. Hergenhahn, J. Electron Spectrosc. Relat. Phenom. **184**, 78 (2011).

[7] T. Jahnke, J. Phys. B: At., Mol. Opt. Phys. **48**, 082001 (2015).

[8] T. Jahnke, U. Hergenhahn, B. Winter, R. Dörner, U. Frühling, P. V. Demekhin, K. Gokhberg, L. S. Cederbaum, A. Ehresmann, A. Knie, and A. Dreuw, Chem. Rev. **120**, 11295 (2020).

[9] N. Sisourat, N. V. Kryzhevoi, P. Kolorenč, S. Scheit, T. Jahnke, and L. S. Cederbaum, Nat. Phys. **6**, 508 (2010).

[10] T. Havermeier, T. Jahnke, K. Kreidi, R. Wallauer, S. Voss, M. Schöffler, S. Schössler, L. Foucar, N. Neumann, J. Titze *et al.*, Phys. Rev. Lett. **104**, 133401 (2010).

[11] R. Santra, J. Zobeley, L. S. Cederbaum, and N. Moiseyev, Phys. Rev. Lett. **85**, 4490 (2000).

[12] R. Santra, J. Zobeley, and L. S. Cederbaum, Phys. Rev. B **64**, 245104 (2001).

[13] I. B. Müller and L. S. Cederbaum, J. Chem. Phys. **125**, 204305 (2006).

[14] M. Mucke, M. Braune, S. Barth, M. Förstel, T. Lischke, V. Ulrich, T. Arion, U. Becker, A. Bradshaw, and U. Hergenhahn, Nat. Phys. **6**, 143 (2010).

[15] T. Jahnke, H. Sann, T. Havermeier, K. Kreidi, C. Stuck, M. Meckel, M. Schöffler, N. Neumann, R. Wallauer, S. Voss *et al.*, Nat. Phys. **6**, 139 (2010).

[16] P. H. P. Harbach, M. Schneider, S. Faraji, and A. Dreuw, J. Phys. Chem. Lett. **4**, 943 (2013).

[17] E. Alizadeh, T. M. Orlando, and L. Sanche, Annu. Rev. Phys. Chem. **66**, 379 (2015).

[18] X. Ren, E. Wang, A. D. Skitnevskaya, A. B. Trofimov, K. Gokhberg, and A. Dorn, Nat. Phys. **14**, 1062 (2018).

[19] P. Zhang, C. Perry, T. T. Luu, D. Matselyukh, and H. J. Wörner, Phys. Rev. Lett. **128**, 133001 (2022).

[20] H. C. Schewe, E. Muchová, M. Belina, T. Buttersack, D. Stemer, R. Seidel, S. Thürmer, P. Slavíček, and B. Winter, Struct. Dyn. **9**, 044901 (2022).

[21] I. Cherkes and N. Moiseyev, Phys. Rev. B **83**, 113303 (2011).

[22] A. Bande, K. Gokhberg, and L. S. Cederbaum, J. Chem. Phys. **135**, 144112 (2011).

[23] L. S. Cederbaum and A. I. Kuleff, Nat. Commun. **12**, 4083 (2021).

[24] L. S. Cederbaum, Phys. Rev. Lett. **121**, 223001 (2018).

[25] A. C. LaForge, M. Shcherbinin, F. Stienkemeier, R. Richter, R. Moshammer, T. Pfeifer, and M. Mudrich, Nat. Phys. **15**, 247 (2019).

[26] A. Eckey, A. B. Voitkiv, and C. Müller, J. Phys. B: At., Mol. Opt. Phys. **53**, 055001 (2020).

[27] J. Fedyk, K. Gokhberg, and L. S. Cederbaum, Phys. Rev. A **103**, 022816 (2021).

[28] J. Zhou, X. Yu, S. Luo, X. Xue, S. Jia, X. Zhang, Y. Zhao, X. Hao, L. He, C. Wang, D. Ding, and X. Ren, Nat. Commun. **13**, 5335 (2022).

[29] R. Santra and L. S. Cederbaum, Phys. Rev. Lett. **90**, 153401 (2003).

[30] K. Kreidi, T. Jahnke, T. Weber, T. Havermeier, X. Liu, Y. Morisita, S. Schössler, L. P. H. Schmidt, M. Schöffler, M. Odenweller *et al.*, Phys. Rev. A **78**, 043422 (2008).

[31] P. O'Keeffe, E. Ripani, P. Bolognesi, M. Coreno, M. Devetta, C. Callegari, M. Di Fraia, K. C. Prince, R. Richter, M. Alagia *et al.*, J. Phys. Chem. Lett. **4**, 1797 (2013).

[32] K. Gokhberg, P. Kolorenc, A. I. Kuleff, and L. S. Cederbaum, Nature (London) **505**, 661 (2014).

[33] F. Trinter, M. S. Schöffler, H.-K. Kim, F. P. Sturm, K. Cole, N. Neumann, A. Vredenborg, J. Williams, I. Bocharova, R. Guillemin *et al.*, Nature (London) **505**, 664 (2014).

[34] V. Stumpf, K. Gokhberg, and L. S. Cederbaum, Nat. Chem. **8**, 237 (2016).

[35] I. B. Müller and L. S. Cederbaum, J. Chem. Phys. **122**, 094305 (2005).

[36] J. Zobeley, R. Santra, and L. S. Cederbaum, J. Chem. Phys. **115**, 5076 (2001).

[37] I. Unger, R. Seidel, S. Thürmer, M. N. Pohl, E. F. Aziz, L. S. Cederbaum, E. Muchová, P. Slavíček, B. Winter, and N. V. Kryzhevoi, Nat. Chem. **9**, 708 (2017).

[38] T. Ouchi, H. Fukuzawa, K. Sakai, T. Mazza, M. Schöffler, K. Nagaya, Y. Tamenori, N. Saito, and K. Ueda, Chem. Phys. **482**, 244 (2017).

[39] M. N. Pohl, C. Richter, E. Lugovoy, R. Seidel, P. Slavíček, E. F. Aziz, B. Abel, B. Winter, and U. Hergenhahn, J. Phys. Chem. B **121**, 7709 (2017).

[40] K. Gokhberg and L. S. Cederbaum, J. Phys. B: At., Mol. Opt. Phys. **42**, 231001 (2009).

[41] N. Sisourat, T. Miteva, J. D. Gorfinkiel, K. Gokhberg, and L. S. Cederbaum, Phys. Rev. A **98**, 020701(R) (2018).

[42] H.-K. Kim, H. Gassert, M. S. Schöffler, J. N. Titze, M. Waitz, J. Voigtsberger, F. Trinter, J. Becht, A. Kalinin, N. Neumann *et al.*, Phys. Rev. A **88**, 042707 (2013).

[43] S. Yan, P. Zhang, X. Ma, S. Xu, B. Li, X. L. Zhu, W. T. Feng, S. F. Zhang, D. M. Zhao, R. T. Zhang *et al.*, Phys. Rev. A **88**, 042712 (2013).

[44] S. Yan, P. Zhang, X. Ma, S. Xu, S. X. Tian, B. Li, X. L. Zhu, W. T. Feng, and D. M. Zhao, Phys. Rev. A **89**, 062707 (2014).

[45] F. Grüll, A. B. Voitkiv, and C. Müller, Phys. Rev. A **100**, 032702 (2019).

[46] S. Scheit, L. S. Cederbaum, and H.-D. Meyer, J. Chem. Phys. **118**, 2092 (2003).

[47] S. Scheit, V. Averbukh, H.-D. Meyer, N. Moiseyev, R. Santra, T. Sommerfeld, J. Zobeley, and L. S. Cederbaum, J. Chem. Phys. **121**, 8393 (2004).

[48] K. Schnorr, A. Senftleben, M. Kurka, A. Rudenko, L. Foucar, G. Schmid, A. Broska, T. Pfeifer, K. Meyer, D. Anielski *et al.*, Phys. Rev. Lett. **111**, 093402 (2013).

[49] N. Sisourat, N. V. Kryzhevoi, P. c. v. Kolorenč, S. Scheit, and L. S. Cederbaum, Phys. Rev. A **82**, 053401 (2010).

[50] S. Scheit, V. Averbukh, H.-D. Meyer, J. Zobeley, and L. S. Cederbaum, J. Chem. Phys. **124**, 154305 (2006).

[51] F. Trinter, T. Miteva, M. Weller, A. Hartung, M. Richter, J. B. Williams, A. Gatton, B. Gaire, J. Sartor, A. L. Landers *et al.*, Chem. Sci. **13**, 1789 (2022).
[52] A. Niehaus, J. Phys. B **10**, 1845 (1977).
[53] F. Trinter, J. B. Williams, M. Weller, M. Waitz, M. Pitzer, J. Voigtsberger, C. Schober, G. Kastirke, C. Müller, C. Goihl *et al.*, Phys. Rev. Lett. **111**, 093401 (2013).
[54] R. Dörner, V. Mergel, O. Jagutzki, L. Spielberger, J. Ullrich, R. Moshammer, and H. Schmidt-Böcking, Phys. Rep. **330**, 95 (2000).
[55] F. Kaspar, W. Domcke, and L. Cederbaum, Chem. Phys. **44**, 33 (1979).
[56] S. Scheit and L. S. Cederbaum, Phys. Rev. Lett. **96**, 233001 (2006).
[57] N. Moiseyev, R. Santra, J. Zobeley, and L. S. Cederbaum, J. Chem. Phys. **114**, 7351 (2001).
[58] L. S. Cederbaum and F. Tarantelli, J. Chem. Phys. **98**, 9691 (1993).
[59] E. Pahl, H.-D. Meyer, and L. S. Cederbaum, Z. Phys. D: At., Mol. Clusters **38**, 215 (1996).
[60] Y.-C. Chiang, F. Otto, H.-D. Meyer, and L. S. Cederbaum, J. Chem. Phys. **136**, 114111 (2012).
[61] D. A. Barrow, M. J. Slaman, and R. A. Aziz, J. Chem. Phys. **91**, 6348 (1989).
[62] J. Schirmer, L. S. Cederbaum, and O. Walter, Phys. Rev. A **28**, 1237 (1983).
[63] J. Schirmer, A. B. Trofimov, and G. Stelter, J. Chem. Phys. **109**, 4734 (1998).
[64] V. Averbukh and L. S. Cederbaum, J. Chem. Phys. **123**, 204107 (2005).
[65] J. Schirmer and A. Barth, Z. Phys. A: At. Nucl. **317**, 267 (1984).
[66] J. N. Bardsley, A. Herzenberg, and F. Mandl, Proc. Phys. Soc. **89**, 321 (1966).
[67] T. F. O'Malley, Phys. Rev. **150**, 14 (1966).
[68] L. S. Cederbaum and W. Domcke, J. Phys. B **14**, 4665 (1981).
[69] N. Moiseyev, P. Certain, and F. Weinhold, Mol. Phys. **36**, 1613 (1978).
[70] J. C. Light, I. P. Hamilton, and J. V. Lill, J. Chem. Phys. **82**, 1400 (1985).
[71] Y.-C. Chiang, F. Otto, H.-D. Meyer, and L. S. Cederbaum, Phys. Rev. Lett. **107**, 173001 (2011).
[72] H.-D. Meyer, U. Manthe, and L. Cederbaum, Chem. Phys. Lett. **165**, 73 (1990).
[73] M. Beck, A. Jäckle, G. Worth, and H.-D. Meyer, Phys. Rep. **324**, 1 (2000).
[74] C. Leforestier and R. E. Wyatt, J. Chem. Phys. **78**, 2334 (1983).
[75] U. V. Riss and H. Meyer, J. Chem. Phys. **105**, 1409 (1996).
[76] P. V. Demekhin, Y.-C. Chiang, S. D. Stoychev, P. Kolorenč, S. Scheit, A. I. Kuleff, F. Tarantelli, and L. S. Cederbaum, J. Chem. Phys. **131**, 104303 (2009).
[77] T. Ouchi, K. Sakai, H. Fukuzawa, I. Higuchi, P. V. Demekhin, Y.-C. Chiang, S. D. Stoychev, A. I. Kuleff, T. Mazza, M. Schöffler *et al.*, Phys. Rev. A **83**, 053415 (2011).
[78] V. Averbukh, I. B. Müller, and L. S. Cederbaum, Phys. Rev. Lett. **93**, 263002 (2004).